# Boosting the Reversibility and Kinetics of Anionic Redox Chemistry in Sodium-Ion Oxide Cathodes via Reductive Coupling Mechanism

Yao Wang, Xudong Zhao, Junteng Jin, Qiuyu Shen, Yang Hu, Xiaobai Song, Han Li, Xuanhui Qu, Lifang Jiao, and Yongchang Liu*

ABSTRACT: Activating anionic redox chemistry in layered oxide cathodes is a paradigmatic approach to devise high-energy sodium-ion batteries. Unfortunately, excessive oxygen redox usually induces irreversible lattice oxygen loss and cation migration, resulting in rapid capacity and voltage fading and sluggish reaction kinetics. Herein, the reductive coupling mechanism (RCM) of uncommon electron transfer from oxygen to copper ions is unraveled in a novel P2-$Na_{0.8}Cu_{0.22}Li_{0.08}Mn_{0.67}O_2$ cathode for boosting the reversibility and kinetics of anionic redox reactions. The resultant strong covalent Cu−(O−O) bonding can efficaciously suppress excessive oxygen oxidation and irreversible cation migration. Consequently, the P2-$Na_{0.8}Cu_{0.22}Li_{0.08}Mn_{0.67}O_2$ cathode delivers a marvelous rate capability

Reversible and Rapid Anionic Redox Chemistry

(134.1 and 63.2 mAh g^{-1} at 0.1C and 100C, respectively) and outstanding long-term cycling stability (82% capacity retention after 500 cycles at 10C). The intrinsic functioning mechanisms of RCM are fully understood through systematic in situ/ex situ characterizations and theoretical computations. This study opens a new avenue toward enhancing the stability and dynamics of oxygen redox chemistry.
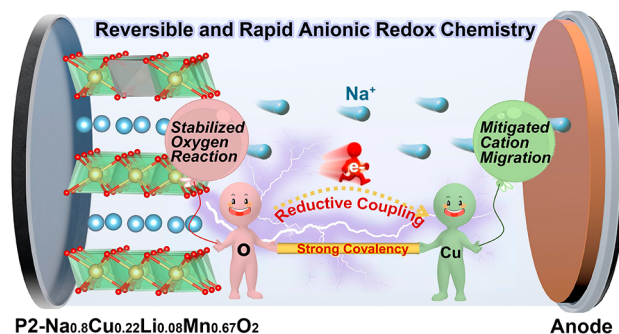
INTRODUCTION

With the rapid development of low-speed electric vehicles and grid-scale energy storage devices, sodium-ion batteries (SIBs) have been considered as a promising complement to lithium-ion batteries (LIBs) owing to the abundant and low-cost sodium resources.[1,2] Nonetheless, the higher redox potential and larger mass/size of Na$^+$ compared with those of Li$^+$ generally result in inferior energy density and sluggish reaction kinetics, hampering the practical applications of SIBs.[3−5] Considering the crucial role of the cathode material in determining the electrochemical performance of battery chemistry, great efforts should be invested to explore high-specific-energy cathodes that can accommodate stable and fast Na-ion storage.[6−8]

Among the studied sodium-storage cathodes, layered transition metal (TM) oxides are appealing candidates because they provide a feasible solution to overcome the energy density dilemma by triggering anionic redox chemistry, especially the low-cost and ecofriendly Mn-rich oxide cathodes.[9−13] However, the inadequate covalency of the TM−O bond (insufficient TM(nd)−O(2p) orbitals overlap) in most anion-redox cathode materials typically induces excessive oxygen oxidation and subsequent irreversible lattice oxygen loss, and then TM migration occurs caused by the lack of coordinating oxygen atoms after O$_2$ release. The above concerns lead to severe structural degradation with rapid

capacity/voltage decay and sluggish reaction kinetics.[14,15] To address these issues, 4d or 5d transition metal doping has been adopted to alleviate the over-reaction of oxygen redox via the formation of strong covalent TM−O bonds (due to the relatively high overlapping degree between TM 4d/5d and O 2p orbitals). For example, Zhou's team prepared an O3-$Na_{1.2}Mn_{0.4}Ir_{0.4}O_2$ cathode, exhibiting an enhanced cycling stability (about 70% capacity retention after 50 cycles) on account of the strong Ir−O covalency.[15] In addition, Liu's group reported that the Li$_2$SiO$_3$ nanolayers coated on the P2-$Na_{0.67}Mn_{0.5}Fe_{0.5}O_2$ cathode could improve the oxygen reaction reversibility, demonstrating a good capacity retention of 80% over 50 cycles.[16] Despite the encouraging advancements, the aforementioned strategies not only inevitably sacrificed a portion of specific capacity but also made the synthesis procedures complicated and costly. Over the past few years, an anomalous phenomenon of electron transfer from oxygen to TM cation (TM reduction) upon electrochemical oxidation, called the reductive coupling mechanism (RCM), was
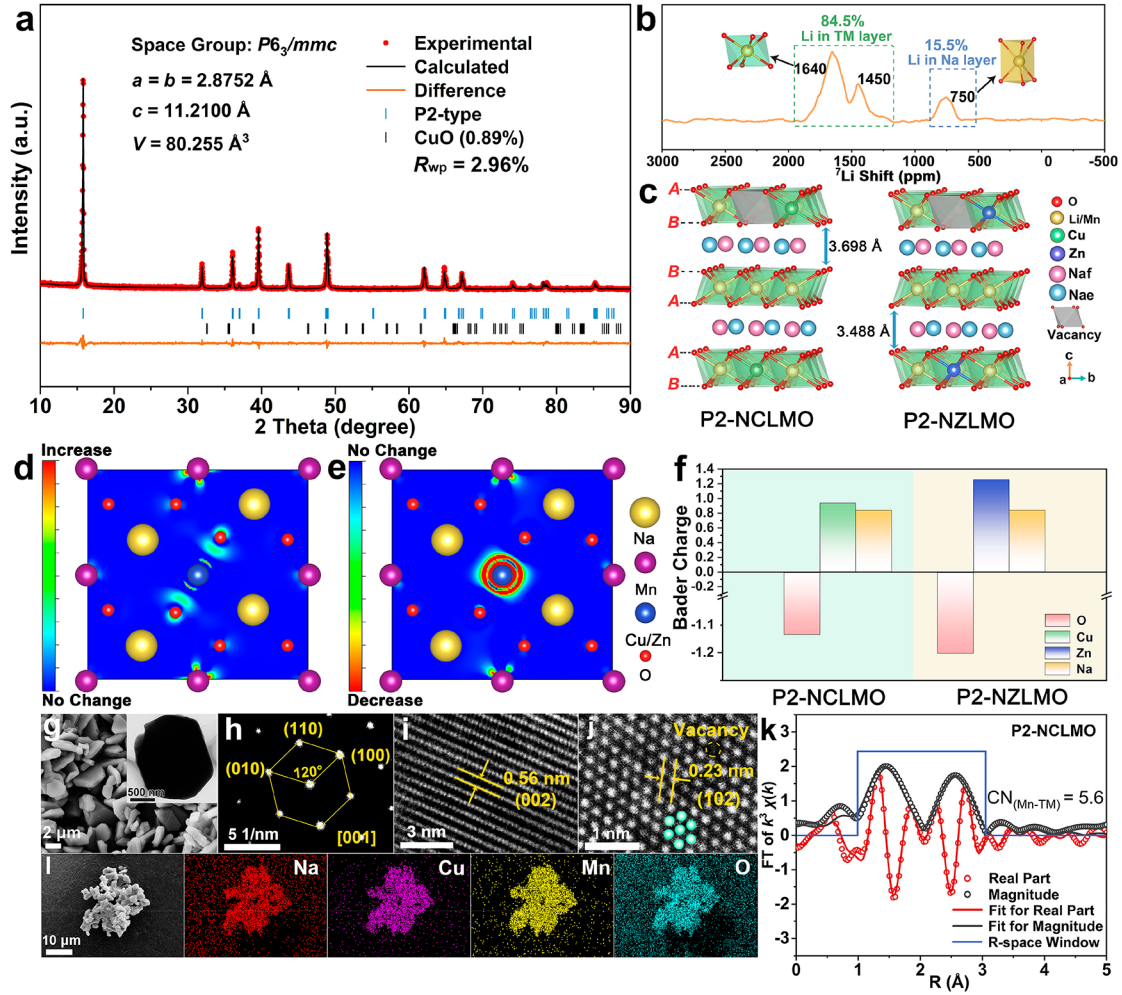
Figure 1. Structure and morphology. (a) Rietveld refined XRD pattern and (b) ^7Li ss-NMR spectrum of the as-synthesized P2-$Na_{0.8}Cu_{0.22}Li_{0.08}Mn_{0.67}O_2$ material. (c) Schematic crystal structures of P2-NCLMO and P2-NZLMO. Charge density difference of Cu replaced by Zn in the oxide system; (d) and (e) represent charge increase and decrease, respectively. (f) Bader charges of the O, Cu, Zn, and Na ions in P2-NCLMO and P2-NZLMO. (g) SEM and TEM (inset) images, (h) SAED pattern, and (i, j) HRTEM images of P2-NCLMO. (k) Fitted Mn K-edge FT-EXAFS spectrum of P2-NCLMO. (l) SEM-EDS mapping images of the P2-NCLMO sample.

pioneeringly observed by Tarascon, Doublet, and co-workers in Li-rich layered oxide cathodes.[17−20] Nevertheless, few studies have focused on the reductive coupling mechanism of sodium-layered oxides to date; particularly, the impact of RCM on the reversibility and dynamics of oxygen redox reaction in sodium oxide cathodes has not been well clarified. It is thereby highly desirable, but remains a big challenge to stimulate the reductive coupling mechanism between the cost-effective 3d TM ions and oxygen to form strong covalent TM−O interactions toward improving the oxygen redox stability and mediating the sluggish anionic process by virtue of the fast-kinetics cationic redox reaction.

Herein, we successfully decipher the underlying reductive coupling mechanism between the 3d Cu ion and oxygen ligand in a novel anion-redox P2-$Na_{0.8}Cu_{0.22}Li_{0.08}Mn_{0.67}O_2$ cathode material (denoted as P2-NCLMO) and break the seemingly inherent connection between oxygen redox reaction and sluggish kinetics. TM vacancy manufacturing and Li doping are designed to trigger oxygen reactivity by creating non-bonding oxygen states. Besides, the low-valence Li$^+$ doping enables the Na-rich character to avoid the gliding of TMO_2 slabs upon charge/discharge. The strong Cu−O covalency can suppress excessive oxygen oxidation and irreversible TM

migration through the reductive coupling mechanism and, meanwhile, leads to a large sodium-layer distance for facile Na$^+$ diffusion owing to the low effective negative charge around O ions, which collaboratively boost the reversibility and kinetics of the anionic reaction. Consequently, the P2-NCLMO cathode delivers a remarkable rate performance (134.1 and 63.2 mAh g^{-1} at 0.1C and 100C, respectively) and outstanding cycling stability (82% capacity retention after 500 cycles at 10C) within 2.0−4.4 V. A complete solid-solution behavior with an ultralow volume variation (1.26%) during the Na$^+$ uptake−release process is demonstrated by operando X-ray diffraction (XRD). Ex situ X-ray absorption spectroscopy (XAS), X-ray photoelectron spectroscopy (XPS), electron energy loss spectroscopy (EELS), and electron paramagnetic resonance (EPR) analyses elucidate the charge transfer mechanism of the cathode upon Na-ion insertion/extraction. Moreover, the rapid Na$^+$ diffusivity was verified by multiple electrochemical measurements cooperating with ex situ Raman spectroscopy. The partial density of states (pDOS) and crystal orbital Hamiltonian population (COHP) are calculated to reveal the electronic structure evolution upon desodiation, and the intrinsic functioning mechanism of RCM for stabilizing the oxygen reaction is fully understood. Finally, prototype sodium-
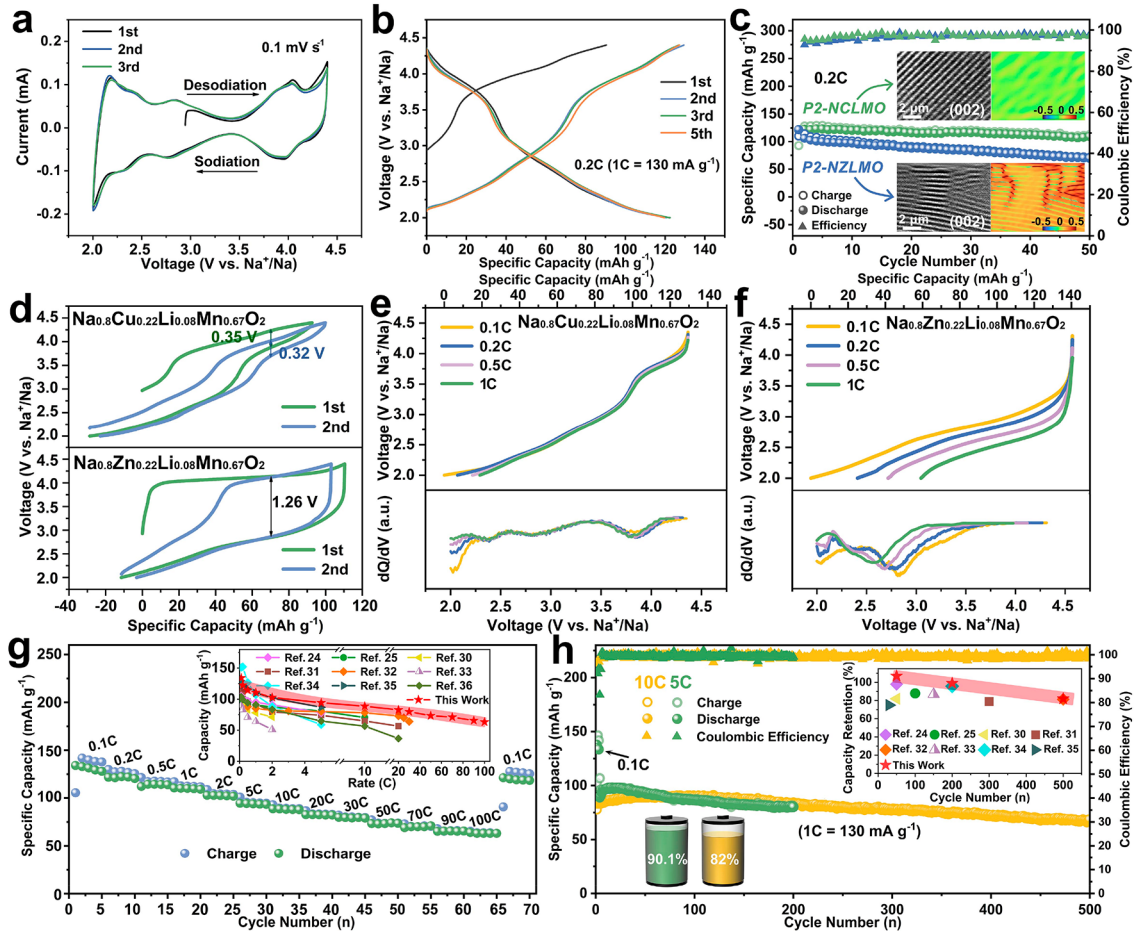
Figure 2. Electrochemical performance. (a) CV profiles at 0.1 mV s^{-1} and (b) galvanostatic charge−discharge curves at 0.2C within 2.0−4.4 V (versus Na$^+$/Na) of the P2-NCLMO cathode. (c) Cycling stability and (d) voltage hysteresis plots at 0.2C of P2-NCLMO and P2-NZLMO. Insets present the HRTEM images of the two samples after 50 cycles and corresponding GPA patterns. Discharge curves and corresponding dQ/dV plots of (e) P2-NCLMO and (f) P2-NZLMO at increasing rates from 0.1C to 1C. (g) Rate performance and (h) long-term cycling durability at 5C and 10C of P2-NCLMO. Insets show the comparison of the present study with the reported Cu−Mn-based sodium layered oxides.

ion full batteries are rationally assembled by pairing the P2-NCLMO cathode with the hard carbon (HC) anode, manifesting bright application prospects.

RESULTS AND DISCUSSION

The P2-type Na$_{0.8}$Cu$_{0.22}$Li$_{0.08}$Mn$_{0.67}$O$_2$ sample featuring strong Cu−O covalency was prepared via a feasible sol−gel method, and the P2-Na$_{0.8}$Zn$_{0.22}$Li$_{0.08}$Mn$_{0.67}$O$_2$ material (denoted as P2-NZLMO) with an ionic Zn−O bond was also synthesized for comparison (Figure S1 and Table S1). The Rietveld refined XRD pattern suggests that the P2-NCLMO material crystallizes in a hexagonal P2 phase (space group: $P6_3/mmc$) with a slight CuO (0.89%) impurity (Figure 1a). The small R factor (R_{wp} = 2.96%) indicates good agreement between the experimental and calculated profiles. Detailed crystallographic information regarding the lattice constants, atomic occupancies, and thermal factors is provided in Table S2. The Rietveld refinement results clarify that Li$^+$ is mainly doped into the TM sites due to their similar ionic radii.[13] This point is also ascertained by the ^{7}Li solid-state nuclear magnetic resonance (ss-NMR) spectrum (Figure 1b), where approximately 84.5% of Li$^+$ ions reside in TM sites (resonance peaks at ≈1640 and ≈1450 ppm, the signal deviation originates from the different amounts of surrounding MnO$_6$ octahedra[21]) and 15.5% in Na sites (resonance peak at ≈750 ppm).[22,23] The crystalline

structures of P2-NCLMO and P2-NZLMO are schematically illustrated in Figure 1c, where the oxygen layers are stacked in an ABBA sequence along the c-axis. Na ions occupy two different prismatic sites, namely, Na$_f$ and Na$_e$ sharing faces and edges with TMO$_6$ octahedra, respectively. Moreover, the refined Na-layer distance of P2-NCLMO (3.698 Å) is larger than that of P2-NZLMO (3.488 Å), which can facilitate Na$^+$ diffusion dynamics. This is because the greater covalency of the Cu−O bond than that of the Zn−O bond would lead to a lower effective negative charge around the O ions, reducing the electrostatic attraction between Na and the O ions and thus leading to a longer Na−O bond. As evidenced by the charge density difference analyses, the charge density of O and Zn ions increases (Figure 1d) and decreases (Figure 1e), respectively, after replacing Cu by Zn in the oxide system, and the Bader charge calculations also give similar results (Figure 1f). Scanning electron microscopy (SEM) and transmission electron microscopy (TEM) images show that the P2-NCLMO material appears as flakelike particles with sizes of 1−5 μm and thicknesses of 0.3−1 μm (Figure 1g and Figure S2), similar to that of P2-NZLMO (Figure S3). The selected area electron diffraction (SAED) pattern along the [001] zone axis exhibits bright diffraction spots, unveiling the single-crystalline hexagonal structure of P2-NCLMO (Figure 1h). Moreover, the well-resolved lattice fringes in the high-
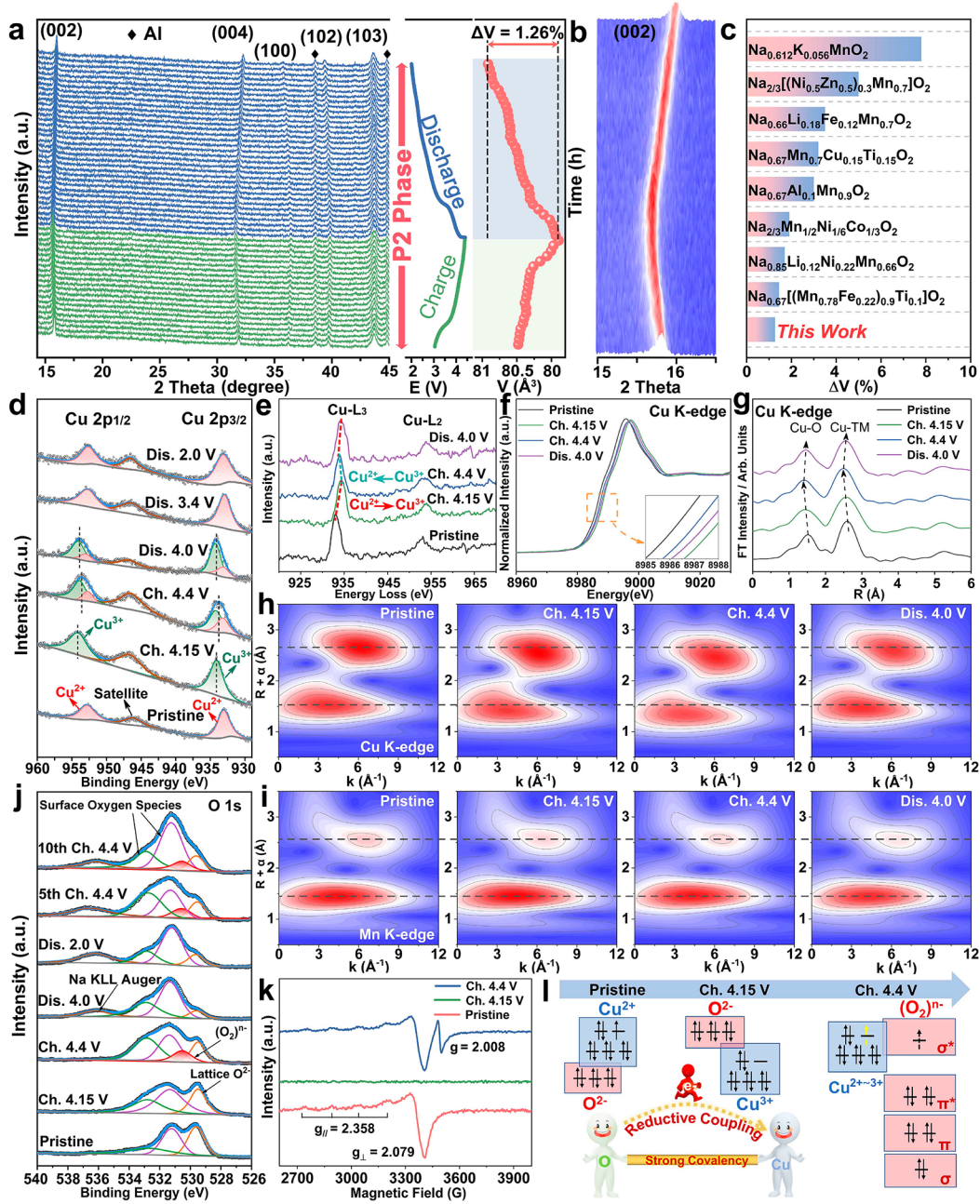
Figure 3. Na-storage mechanisms. (a) In situ XRD patterns and corresponding volume variations of the P2-NCLMO electrode in the first cycle at 0.2C, as well as (b) contour plot of the (002) peak. (c) Comparison of maximum unit cell volume change between the present P2-NCLMO cathode and previously reported P2-type cathodes for SIBs. Ex situ (d) core-level Cu 2p XPS spectra, (e) Cu L-edge EELS spectra, Cu K-edge (f) XANES spectra, and (g) corresponding FT-EXAFS spectra of P2-NCLMO. Contour plots of the (h) Cu and (i) Mn K-edge WT-EXAFS spectra at different voltage states. (j) O 1s XPS spectra of P2-NCLMO at various electrochemical states. (k) EPR spectra of P2-NCLMO at the pristine, charged to 4.15 V, and charged to 4.4 V states. (l) Schematic illustration of the Cu 3d and O 2p orbital electronic configurations' evolution during the initial desodiation process.

resolution TEM (HRTEM) images with interplanar spacings of 0.56 and 0.23 nm correspond to the (002) and (102) planes of the layered structure (Figure 1i,j). Notably, the TM vacancy could be directly observed in the (102) plane. The Mn K-edge Fourier-transformed extended X-ray absorption fine structure (FT-EXAFS) spectrum and the fitting results for P2-NCLMO are shown in Figure 1k and Table S3. Of note, the coordination number (CN) of the Mn−TM interaction in the second coordination shell is 5.6, which is lower than 6.0 for the standard hexagonal coordination value, further confirming the existence of TM vacancies. The homogeneous distribution

of Na, Cu, Mn, and O elements throughout the P2-NCLMO particles is revealed by SEM energy dispersive spectroscopy (EDS) mapping (Figure 1l). Inductively coupled plasma mass spectroscopy (ICP-MS, Table S4), XPS survey spectrum (Figure S4), and TEM-EDS analyses (Figure S5) further prove the existence of Na, Cu, Li, Mn, and O in P2-NCLMO without any other impurity element, and their molar ratio conforms well with the anticipated value, reflecting the good purity of the as-prepared product.

The electrochemical properties of P2-NCLMO and P2-NZLMO were systematically evaluated in Na half-cells

between 2.0 and 4.4 V versus Na$^+$/Na. Figure 2a plots the cyclic voltammetry (CV) profiles at a sweep rate of 0.1 mV s^{-1} of P2-NCLMO, and five couples of stepwise redox peaks located at 2.18/2.00, 2.44/2.35, 2.83/2.77, 4.03/3.91, and 4.40/4.27 V are discerned. The peaks centered at 4.03/3.91 V and 4.40/4.27 V are assigned to Cu^{2+}/Cu^{3+} and O^{2-}/(O$_2$)$^{n-}$ redox reactions, respectively, and the peaks below 3.4 V are associated with the Mn^{3+}/Mn^{4+} redox couple (as will be demonstrated later).[24,25] The well-overlapped CV plots imply highly reversible redox reactions accompanied by repeated Na$^+$ insertion/extraction. The P2-NCLMO electrode affords an initial charge capacity of 90.4 mAh g^{-1} at 0.2C (1C = 130 mA g^{-1}, Figure 2b), which corresponds to about a 0.34-electron transfer (Figure S6) and exceeds the theoretical capacity based on the oxidation of Cu^{2+} to Cu^{3+} (0.22-electron transfer per formula unit). Since the tetravalent Mn cannot be further oxidized and the employed electrolyte decomposes above 4.5 V (Figure S7), the extra capacity should be attributed to the oxidation of oxygen.[26] Furthermore, the overlapping charge/discharge curves in the high-voltage region reflect the stable anionic redox chemistry in the P2-NCLMO cathode, which benefits from the strong covalency between the Cu 3d and the O 2p states. As for the P2-NZLMO electrode, the extremely sharp but significantly reduced oxygen oxidation peak in CV profiles upon cycling coincides with the gradually decreased charge plateau in voltage profiles (Figure S8), manifesting stronger but irreversible oxygen redox activity. This phenomenon can be interpreted as that the strong ionic Zn–O bond would induce lattice oxygen loss after contributing excessive electrons.[27] The cycling performance and corresponding average discharge voltage variation of P2-NCLMO and P2-NZLMO electrodes at 0.2C are depicted in Figure 2c and Figure S9. The P2-NCLMO cathode yields a promising capacity retention of 90.3% over 50 cycles as well as a higher and more stable average discharge voltage, while the P2-NZLMO electrode shows rapid capacity fading with only 57.2% capacity retention and serious voltage degradation after 50 cycles. Post-mortem HRTEM images and corresponding geometric phase analysis (GPA) patterns (insets of Figure 2c) reveal that the layered structure of P2-NCLMO is well maintained after cycling with small and uniform internal strain, while the internal strain in P2-NZLMO is huge and intensive, accompanied by severe lattice distortions and particle cracks (Figure S10). The above results attest that the strong Cu–O covalency could suppress the irreversible oxygen release and ensure structural integrity. The enhanced lattice oxygen stability of P2-NCLMO was also confirmed by the differential scanning calorimetry (DSC) analyses (Figure S11).

In addition, the severe voltage hysteresis is another fatal problem facing oxygen redox reactions that deteriorates electrochemical performance.[14,28,29] Intriguingly, the P2-NCLMO cathode shows much lower voltage hysteresis compared with that of P2-NZLMO in the high-voltage region (Figure 2d), unambiguously validating the improved anionic redox kinetics.[14,26] This fact is further verified by rate capability tests (Figure 2e,f). The P2-NCLMO electrode displays overlapping discharge profiles, and the corresponding differential capacity versus voltage (dQ/dV) peaks at high voltages fit well as the C rate increases, whereas the P2-NZLMO electrode shows rapid discharge capacity decay and obviously decreased dQ/dV peak intensities with the increase of C rate. This is because the anionic reaction in P2-NCLMO is mediated by the fast-kinetic cationic reaction (Cu^{2+}/Cu^{3+}).

Besides, the strong Cu–O covalency could effectively mitigate the TM migration via a reductive coupling mechanism, thus facilitating the Na$^+$ diffusion dynamics (as will be discussed later). As a result, the P2-NCLMO cathode delivers admirable discharge capacities of 134.1 mAh g^{-1} at 0.1C and 63.2 mAh g^{-1} even at 100C (Figure 2g), which break the conventional perception that anion-redox cathodes usually suffer from poor rate performance. By contrast, the P2-NZLMO cathode delivers an inferior rate capability due to the sluggish anionic reaction kinetics (Figure S12). Moreover, the long-term cycling life of P2-NCLMO is presented in Figure 2h, demonstrating respectable capacity retentions of 90.1% after 200 cycles at 5C and 82% after 500 cycles at 10C. The capacity increase during the initial several cycles is related to an electrode activation process, which is confirmed by the electrochemical impedance spectra in Figure S13. As highlighted in the insets of Figure 2g,h and Table S5, the rate performance and cyclic stability of the present P2-NCLMO cathode strikingly stand out among those of the reported Cu–Mn-based sodium oxides and other Na-ion layered oxide cathodes involving anionic redox chemistry.[13,24–26,30–39]

In situ XRD measurement was conducted over the voltage range of 2.0–4.4 V to investigate the structural evolution of P2-NCLMO (Figure 3a,b). During the charge process, the (00l) peaks gradually shift to lower-angle regions, illustrating the expanded interlayer spacing because of the increased electrostatic repulsion between neighboring oxygen slabs after Na$^+$ extraction. Meanwhile, the (10l) peaks continuously move toward higher angles, suggesting the contraction of the ab plane owing to the oxidation of TM ions. In the following discharge process, all the diffraction peaks experience reversible movements, and the (00l) and (10l) peaks shift to higher and lower angles compared with the pristine state, respectively, due to more inserted Na$^+$ ions than the extracted ones in the initial cycle. Notably, no additional peak emerges or the primordial peak vanishes/splits during the whole charge/discharge process, manifesting a highly stable solid-solution reaction of the P2-NCLMO electrode. This is because the low-valence Li$^+$ doping ensures enough sodium is left in Na layers to stabilize the P2 structure at the deep charged state and effectively mitigate the Na$^+$/vacancy ordering.[26,40] Meanwhile, the ICP-MS result (Table S6) and ^{7}Li ss-NMR spectrum (Figure S14) of the fully charged electrode suggest that the stable Li ions in Na sites could serve as rigid LiO$_6$ pillars to suppress the TMO$_2$ slabs' sliding and phase transition.[41] The continuous lattice constant variation extracted from the operando XRD patterns is presented in Figure S15. Intriguingly, the maximum unit cell volume change of P2-NCLMO is merely 1.26%, which is much smaller than those of the previously reported P2-type sodium-ion oxide cathodes (Figure 3c),[22,40,42–45] accounting for the excellent cycling stability of P2-NCLMO.

The charge compensation mechanism of the P2-NCLMO cathode was systematically unveiled via ex situ XAS, XPS, EELS, and EPR analyses. Figure 3d shows the Cu 2p XPS spectra in different electrochemical states. The Cu 2p$_{1/2}$ (952.8 eV) and Cu 2p$_{3/2}$ (933.1 eV) peaks (accompanied by a satellite peak) of the pristine electrode imply the bivalence of copper. Upon charging to 4.15 V, the Cu 2p$_{1/2}$ and Cu 2p$_{3/2}$ peaks shift to higher binding energies of 954.2 and 934.1 eV, respectively, revealing the entire oxidation of Cu^{2+} to Cu^{3+}.[24,31] Unexpectedly, the Cu^{2+} species reappear when fully charged to 4.4 V, indicative of the partial reduction of Cu ions. Such a counterintuitive TM reductive behavior upon charging to high
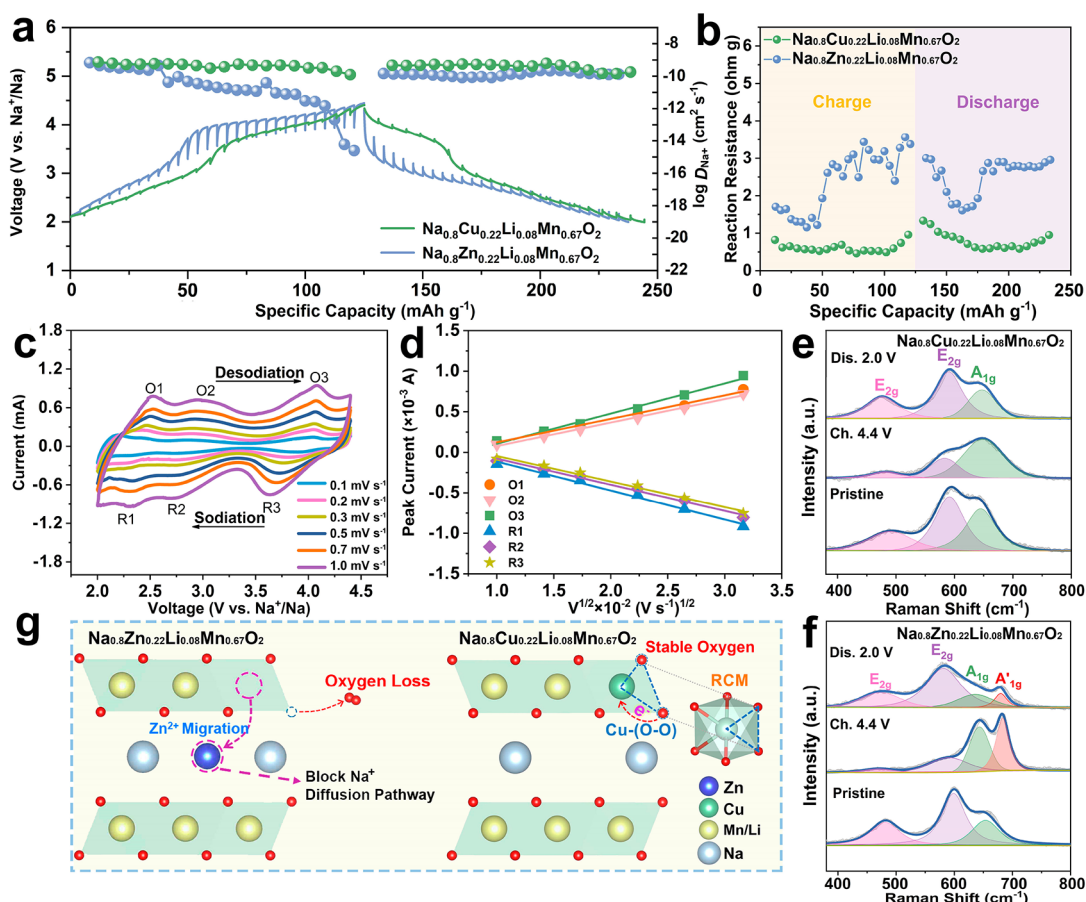
Figure 4. Electrode process kinetics. (a) Charge−discharge GITT plots at 0.2C and corresponding Na⁺ diffusion coefficients of the P2-NCLMO and P2-NZLMO electrodes. (b) Reaction resistances obtained from the GITT results. (c) CV profiles at different scan rates from 0.1 to 1.0 mV s⁻¹ of P2-NCLMO and (d) the liner relationships between peak currents (i_p) and the square root of scan rates ($v^{1/2}$). Ex situ Raman spectra of (e) P2-NCLMO and (f) P2-NZLMO. (g) Illustration of the enhanced reaction kinetics caused by the reductive coupling mechanism.

voltages provides experimental evidence for the reductive coupling mechanism. The Cu 2p peaks abnormally move to higher energies when discharged to 4.0 V concomitant with the return of electrons to the O ion and then recover to the pristine state upon discharging to 3.4 V, suggesting the highly reversible reductive coupling mechanism of Cu ions. The ex situ Mn 2p XPS spectra show that the pristine tetravalent Mn ions, mainly controlled by the low-valence Li⁺ and Cu²⁺ ion doping, are electrochemically inactive during the initial charge process but contribute to the charge compensation in the low-voltage region (Figure S16). It is noteworthy that the average Mn valence state when discharged to 2.0 V during cycling is relatively high, indicating the weak Jahn−Teller effect in P2-NCLMO. In addition, ex situ EELS tests were conducted to monitor the valence variations of Cu and Mn ions upon charge/discharge, and the results agree well with the ex situ XPS observations (Figure 3e and Figure S17; detailed discussion is given in the Supporting Information). Ex situ XAS was further employed to probe the electronic structure changes of P2-NCLMO. The normalized X-ray absorption near-edge structure (XANES) and EXAFS spectra at the Cu K-edge are displayed in Figure 3f,g. Upon charging to 4.15 V, the Cu K-edge XANES spectrum significantly shifts to a higher energy, and the first Cu−O coordination shell obviously shrinks, indicating the oxidation of Cu²⁺. Intriguingly, the Cu K-edge spectrum moves toward a lower energy with a decreased Cu−O distance when fully charged to 4.4 V. This

is because of the formation of the highly covalent Cu−(O−O) bonding (as will be validated later) through the electron transfer from oxygen to copper ions at the deep desodiation state, which is congruent with the XPS and EELS results. When discharged to 4.0 V, such Cu−(O−O) bonding vanishes as the electron returns to oxygen, leading to partial oxidation of Cu ions and the increased Cu−O distance. The second Cu−TM coordination shell undergoes a similar variation due to the edge-shared octahedral structure.[34] As for the Mn ions, no obvious change can be detected in either XANES or EXAFS spectra (Figure S18), suggesting that Mn ions are not involved in the redox reaction at these selected voltage states. The wavelet-transformed (WT) EXAFS spectra at Cu and Mn K-edges (Figure 3h,i) were also recorded to intuitively show the bond length variations during the charge/discharge process, where the two scattering peaks at around 1.5 and 2.5 Å correspond to the TM−O and TM−TM bonds, respectively.

To investigate the contribution of oxygen redox in the charge compensation process, ex situ O 1s XPS spectra were collected (Figure 3j). Three deconvoluted peaks centered at 529.5 eV (lattice oxygen), 531.3, and 532.8 eV (surface oxygen species) are observed in the pristine sample.[13,46] When fully charged to 4.4 V, a new peak at 530.5 eV assigned to the $(O_2)^{n-}$ species emerges, indicating the oxidation of oxygen.[26,41] This peak vanishes during the discharge process and can be detected again in the fully charged state, even after 10 cycles. By quantitatively comparing the $(O_2)^{n-}$ proportions in
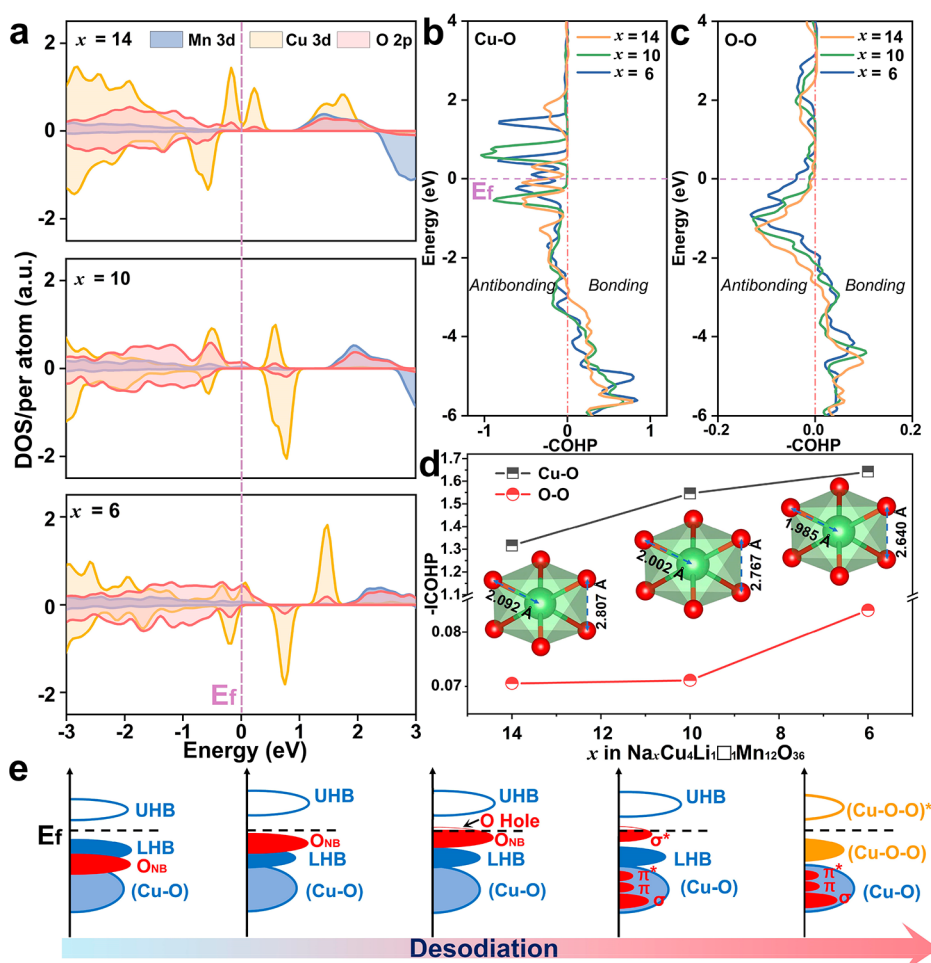
Figure 5. Theoretical computations. (a) pDOS of the $Na_xCu_4Li_1\square_1Mn_{12}O_{36}$ (x = 14, 10, 6) supercells. (b) Cu−O and (c) O−O COHP profiles with (d) corresponding −ICOHP values of $Na_xCu_4Li_1\square_1Mn_{12}O_{36}$ (x = 14, 10, 6). Insets present the local environment evolution of Cu ions (Cu−O and O−O bond distances) derived from DFT calculations. (e) Schematic band diagrams of P2-NCLMO during the desodiation process (O_{NB} represents the nonbonding O 2p states; UHB and LHB represent the upper and lower Hubbard bands, respectively).

the fully charged P2-NCLMO and P2-NZLMO electrodes during cycling (Figure S19), it can be concluded that the oxygen redox reaction in P2-NCLMO possesses a higher reversibility. This point is also verified by the O K-edge EELS spectra of P2-NCLMO (Figure S20), in which the pre-edge peak broadens (oxygen oxidation) when charged to 4.4 V and is restored to the pristine shape (oxygen reduction) after being discharged to 4.0 V.[43] The oxygen redox reactivity and the reductive coupling mechanism of Cu ions are further corroborated by fine-scanning ex situ EPR spectra. As manifested in Figure 3k, the EPR spectrum of the pristine sample features an anisotropic line shape centered at g = 2.079 with four hyperfine lines arising from the coupling between electronic spin S = 1/2 and nuclear spin I = 3/2 of Cu^{2+} ($3d^9$). When charged to 4.15 V, no EPR signal can be detected due to the formation of the EPR-silent Cu^{3+} ($3d^8$).[47] Noticeably, the Cu^{2+} resonance reappears and a new $(O_2)^{n-}$ signal (g = 2.008) is clearly observed after fully charging to 4.4 V,[21,48] coinciding well with the ex situ XPS, EELS, and XANES results. In light of the above analyses, the electronic structure evolution of Cu 3d and O 2p orbitals during the desodiation process is schematically illustrated in Figure 3l, which vividly describes the reductive coupling mechanism of charge transfer from O to Cu to form the Cu−(O−O) configuration in the P2-NCLMO cathode.

To examine the reaction kinetics behind the superb rate capability of P2-NCLMO, multiple electrochemical measurements and ex situ Raman spectroscopy were performed. The galvanostatic intermittent titration technique (GITT) was adopted to evaluate the Na^+ diffusion coefficients (D_{Na}, Figure 4a and Figure S21). The D_{Na} values of P2-NCLMO are calculated to stay at the magnitude of 10^{-10} cm^2 s^{-1} (calculation details in Supporting Information), which are much higher than those of P2-NZLMO (10^{-15}−10^{-10} cm^2 s^{-1}) and other sodium-layered oxide cathodes featuring anionic redox chemistry (mainly in the range of 10^{-12}−10^{-11} cm^2 s^{-1}).[26,40,43,49−51] The reaction resistances obtained from the GITT results are depicted in Figure 4b, where the P2-NCLMO presents much lower values than those of P2-NZLMO during the whole charge/discharge process. Notably, the particularly higher D_{Na} values and lower reaction resistances in the high-voltage region indicate the facilitated oxygen reaction dynamics of P2-NCLMO. The CV curves of P2-NCLMO at different scan rates (0.1 to 1.0 mV s^{-1}) were also recorded to estimate the Na-ion diffusivity (Figure 4c,d). As calculated, the D_{Na} values of O1, O2, O3, R1, R2, and R3 peaks are 1.77 × 10^{-10}, 1.76 × 10^{-10}, 2.63 × 10^{-10}, 2.46 × 10^{-10}, 2.19 × 10^{-10}, and 2.09 × 10^{-10} cm^2 s^{-1}, respectively (calculation details are described in Supporting Information), matching well with the GITT results. Given that the irreversible cation migration
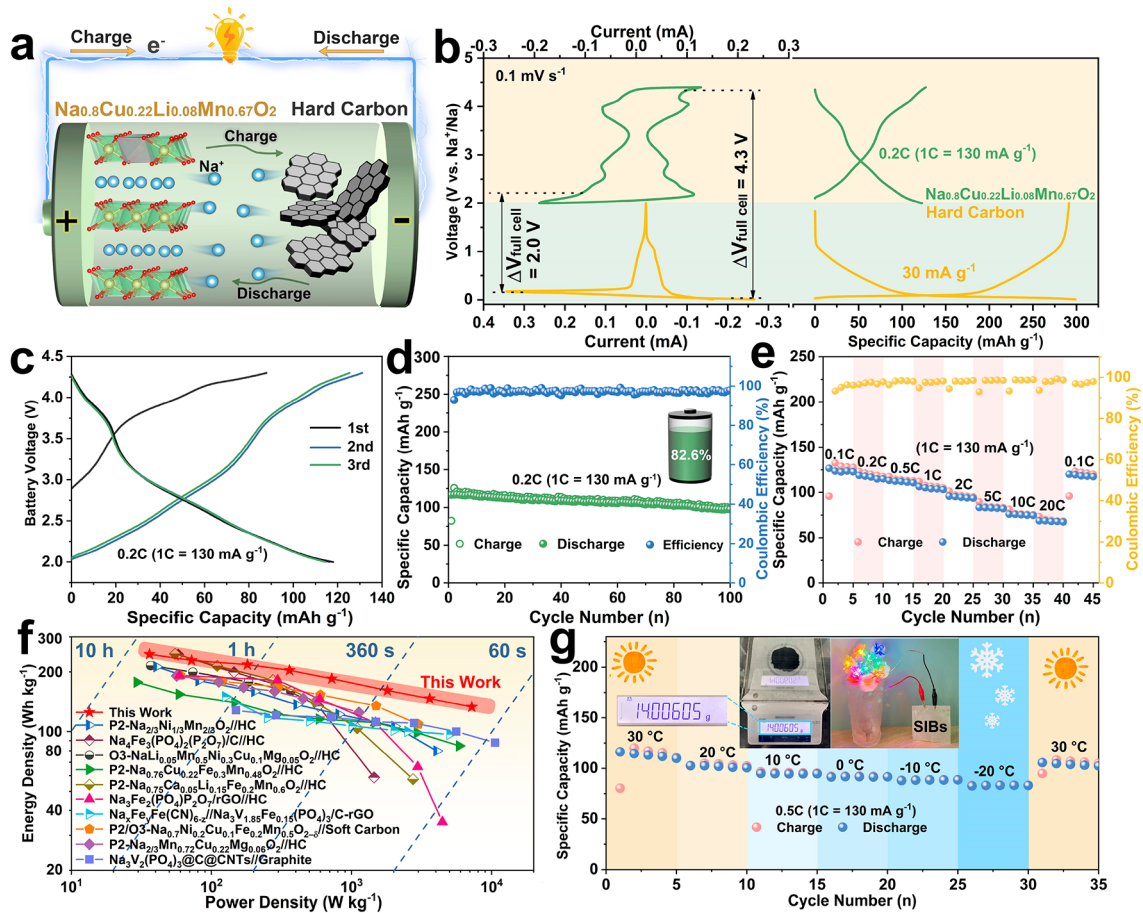
Figure 6. Na-ion full batteries. (a) Schematic diagram of the P2-NCLMO//hard carbon full cell. (b) Cyclic voltammograms and charge−discharge profiles of the P2-NCLMO cathode and HC anode. (c) Galvanostatic charge−discharge curves, (d) cycling performance, and (e) rate capability of the full battery. (f) Ragone plots of the present P2-NCLMO//hard carbon full battery and recently reported Na-ion full cell systems (based on the total mass of cathode and anode). (g) Specific capacities of the full cell at different temperatures. Insets display mass production of the P2-NCLMO cathode material and the LEDs powered by the pouch cell.

is a common issue facing layered oxide cathodes with anionic redox activity,[9,14,52−54] ex situ Raman spectroscopy was carried out to study the TM migration behaviors in P2-NCLMO and P2-NZLMO. The peaks located at ≈490 and ≈590 cm^{-1} are attributed to the asymmetric stretching (E_{2g}) of the Na−O bond, and the peak at ≈650 cm^{-1} arises from the symmetric stretching (A_{1g}) of the TM−O bond.[55] As displayed in Figure 4e, the intensities of the E_{2g} peaks obviously decrease upon desodation and increase upon sodiation, whereas the TM−O vibration of P2-NCLMO shows no apparent change during the charge−discharge process, indicating the well-maintained TM local environment. Together with the ex situ ^{7}Li ss-NMR results (Figure S14), it is concluded that the metal ion migration was efficiently mitigated in P2-NCLMO. By contrast, a new sharp peak (A'_{1g}) appears at ≈680 cm^{-1} when the P2-NZLMO cathode was fully charged to 4.4 V, which is ascribed to the out-of-plane cation migration with the formation of a new TM local environment (Figure 4f).[9] Upon discharging to 2.0 V, this peak still exists, validating the irreversible Zn ion migration from TM layer to Na layer in P2-NZLMO.[27,49] Such serious Zn^{2+} migration caused by the weakened Zn−O coordination after excessive oxygen oxidation leads to the blocked Na$^+$ diffusion pathways and the following drop of Na-ion diffusivity, thus resulting in sluggish reaction kinetics and poor rate performance, as schematically illustrated

in Figure 4g. For the P2-NCLMO electrode, the formation of the stable Cu−(O−O) configuration associated with reductive coupling mechanism accounts for the restrained TM migration, rapid Na-ion diffusivity, and desirable rate capability.

To better understand the critical role of the reductive coupling mechanism in stabilizing oxygen reactions, the pDOS and COHP calculations based on density functional theory (DFT) were carried out on a series of $Na_xCu_4Li_1\square_1Mn_{12}O_{36}$ (x = 14, 10, 6, $\square$ represents vacancy) supercells. The most stable crystal structures of the supercells applied in simulations are illustrated in Figure S22. As shown in Figure 5a, in the case of x = 14, the valence bands in the vicinity of the Fermi level (E_f) are predominantly occupied by Cu 3d orbitals, implying that Cu redox dominates the charge compensation at the beginning of charge. When x = 10, the upper valence bands near E_f are primarily comprised of O 2p states, suggesting that oxygen redox takes over the charge compensation at this stage. Moreover, the Cu 3d valence band neighboring E_f decreases obviously, further manifesting the oxidation of Cu ions during x = 14−10. When x = 6, the O 2p states above E_f (hole densities) significantly increase; meanwhile, an increment in Cu 3d states below E_f is witnessed, indicating the charge transfer from oxygen to Cu ions (reductive coupling mechanism) at the deep desodation state. The pDOS results were also validated by the more sophisticated meta-generalized

gradient approximation (meta-GGA, Figure S23) method, ensuring the authenticity of the conclusions. In addition, the Cu−O and O−O bonding information was investigated through the COHP calculations (Figure 5b,c), where the positive and negative COHP values correspond to the antibonding and bonding states, respectively.[34] As displayed in the Cu−O COHP profiles, the high antibonding participation during the entire desodiation process reflects the strong Cu−O interactions, which are beneficial for stabilizing the oxygen oxidation reaction.[34,56] The integrated COHP (ICOHP) was then used to evaluate the bonding strength of the Cu−O and the O−O bonds (Figure 5d). During $x = 14−10$, the increased −ICOHP value of the Cu−O bond is mainly contributed by the oxidation of Cu^{2+} to Cu^{3+}, conforming well with the shortened Cu−O distance. As for the O−O bond, the relatively low −ICOHP values and long O−O distances suggest almost no bonding interaction between adjacent oxygen ions. With further extraction of Na^+, the increased −ICOHP values of both Cu−O and O−O bonds along with their decreased bond lengths indicate the formation of the stable Cu−(O−O) configuration through the reductive coupling mechanism, in which oxygen ions are covalently bonded to Cu ions.[57] The relatively small change in Cu−O bond length during $x = 10−6$ is attributed to the combined effect of the opposite two aspects: the reduction of Cu ions leads to an increased bond length, while the formation of Cu−(O−O) results in a decreased Cu−O distance. Such a Cu−(O−O) interaction can effectively enhance the stability of oxygen reaction chemistry, as evidenced by the existing experimental results. Accordingly, the charge transfer process and reductive coupling mechanism in P2-NCLMO upon desodiation are illustrated by the schematic band diagrams in Figure 5e (detailed discussion is given in the Supporting Information).

To explore the practical applicability of P2-NCLMO, a sodium-ion full battery was constructed employing the P2-NCLMO cathode and hard carbon (HC) anode (Figure 6a). Based on the CV and charge/discharge profiles of the two paired electrodes (Figure 6b, detailed Na-storage properties of HC are provided in Figure S24), the full-cell voltage window was set to 2.0−4.3 V and the active mass ratio of the anode to cathode was fixed at 1:2.3. Figure 6c,d display the galvanostatic charge−discharge curves and cycling life of the full battery, and a reversible capacity of 117.9 mAh g^{-1} at 0.2C (based on the cathode) with an average working voltage of 2.78 V is achieved, corresponding to a high energy density of 228.4 Wh kg^{-1} based on the total mass of positive and negative electrodes. After 100 cycles, a respectable capacity retention of 82.6% is obtained. Moreover, the full cell affords an excellent rate performance of 126.6 mAh g^{-1} at 0.1C and 68.7 mAh g^{-1} at 20C (Figure 6e). As highlighted in Figure 6f, the full battery exerts great superiority in energy density and power density compared with other recently reported sodium-ion full cells.[25,26,31,58−60] Intriguingly, the present full cell can operate well even at low temperatures (71.5% capacity retention at −20 °C compared to that at 30 °C, Figure 6g and Figure S25), and the pouch battery built by the mass-produced cathode material can continuously power the light-emitting diodes (LEDs, insets of Figure 6g and Figure S26), manifesting the great application potential of the tailored P2-NCLMO cathode.

CONCLUSION

In summary, the underlying reductive coupling mechanism of uncommon electron transfer from the O to Cu ions for enhancing the reversibility and kinetics of the anionic redox reaction was unveiled in a novel P2-$Na_{0.8}Cu_{0.22}Li_{0.08}Mn_{0.67}O_2$ cathode. The strong Cu−O covalency could inhibit excessive oxygen oxidation via the formation of a stable Cu−(O−O) interaction. Therefore, the lattice oxygen loss and irreversible TM migration are restrained simultaneously, which endow the P2-NCLMO electrode with remarkable cycling stability (82% capacity retention after 500 cycles) and exceptional high-rate capability (134.1 mAh g^{-1} at 0.1C and 63.2 mAh g^{-1} at 100C). In situ XRD reveals that P2-NCLMO undergoes an absolute solid-solution reaction with an ultralow volume change of 1.26% during the Na^+ extraction/insertion process. Besides, the rapid electrode kinetics are substantiated by the GITT, CV, and ex situ Raman spectroscopy measurements. More excitingly, the charge transfer mechanism is uncovered by systematic ex situ XAS, XPS, XANES, EELS, and EPR characterizations, and the intrinsic functioning mechanism of RCM for stabilizing anionic redox chemistry is elucidated by DFT calculations. Finally, the prototype sodium-ion full cells assembled by the P2-NCLMO cathode and HC anode exhibit great application prospects in terms of outstanding energy/power density and superb all-climate tolerance. This study offers deep insights into the collaborative anionic and cationic redox chemistry and sheds new light on the development of high-energy layered oxide cathodes for SIBs.

AUTHOR INFORMATION

Corresponding Author

Yongchang Liu − *Beijing Advanced Innovation Center for Materials Genome Engineering, Institute for Advanced Materials and Technology, State Key Laboratory for Advanced Metals and Materials, University of Science and Technology Beijing, Beijing 100083, China; Key Laboratory of Advanced Energy Materials Chemistry (Ministry of Education), Nankai University, Tianjin 300071, China;* orcid.org/0000-0003-1998-9309; Email: liuyc@ustb.edu.cn

Authors

Yao Wang − *Beijing Advanced Innovation Center for Materials Genome Engineering, Institute for Advanced Materials and Technology, State Key Laboratory for Advanced Metals and Materials, University of Science and Technology Beijing, Beijing 100083, China*

Xudong Zhao − *Tianjin Key Laboratory for Photoelectric Materials and Devices, School of Materials Science and*

Engineering, Tianjin University of Technology, Tianjin 300384, China

Junteng Jin − *Beijing Advanced Innovation Center for Materials Genome Engineering, Institute for Advanced Materials and Technology, State Key Laboratory for Advanced Metals and Materials, University of Science and Technology Beijing, Beijing 100083, China*

Qiuyu Shen − *Beijing Advanced Innovation Center for Materials Genome Engineering, Institute for Advanced Materials and Technology, State Key Laboratory for Advanced Metals and Materials, University of Science and Technology Beijing, Beijing 100083, China*

Yang Hu − *Helmholtz Institute Ulm (HIU), Ulm 89081, Germany;* orcid.org/0000-0001-6864-6498

Xiaobai Song − *Beijing Advanced Innovation Center for Materials Genome Engineering, Institute for Advanced Materials and Technology, State Key Laboratory for Advanced Metals and Materials, University of Science and Technology Beijing, Beijing 100083, China*

Han Li − *Beijing Advanced Innovation Center for Materials Genome Engineering, Institute for Advanced Materials and Technology, State Key Laboratory for Advanced Metals and Materials, University of Science and Technology Beijing, Beijing 100083, China*

Xuanhui Qu − *Beijing Advanced Innovation Center for Materials Genome Engineering, Institute for Advanced Materials and Technology, State Key Laboratory for Advanced Metals and Materials, University of Science and Technology Beijing, Beijing 100083, China*

Lifang Jiao − *Key Laboratory of Advanced Energy Materials Chemistry (Ministry of Education), Nankai University, Tianjin 300071, China;* orcid.org/0000-0002-4676-997X

Author Contributions

Y.W. and X.Z. contributed equally to this work. The manuscript was written through contributions of all authors. All authors have given approval to the final version of the manuscript.

Notes

The authors declare no competing financial interest.

ACKNOWLEDGMENTS

REFERENCES

(1) Liu, Q.; Hu, Z.; Li, W.; Zou, C.; Jin, H.; Wang, S.; Chou, S.; Dou, S.-X. Sodium Transition Metal Oxides: The Preferred Cathode Choice for Future Sodium-Ion Batteries? *Energy Environ. Sci.* **2021**, *14*, 158−179.

(2) Yang, C.; Xin, S.; Mai, L.; You, Y. Materials Design for High-Safety Sodium-Ion Battery. *Adv. Energy Mater.* **2021**, *11*, No. 2000974.

(3) Hwang, J.-Y.; Myung, S.-T.; Sun, Y.-K. Sodium-Ion Batteries: Present and Future. *Chem. Soc. Rev.* **2017**, *46*, 3529−3614.

(4) Vaalma, C.; Buchholz, D.; Weil, M.; Passerini, S. A Cost and Resource Analysis of Sodium-Ion Batteries. *Nat. Rev. Mater.* **2018**, *3*, 18013.

(5) Delmas, C. Sodium and Sodium-Ion Batteries: 50 Years of Research. *Adv. Energy Mater.* **2018**, *8*, No. 1703137.

(6) Liu, Y.; Li, J.; Shen, Q.; Zhang, J.; He, P.; Qu, X.; Liu, Y. Advanced Characterizations and Measurements for Sodium-Ion Batteries with NASICON-Type Cathode Materials. *eScience* **2022**, *2*, 10−31.

(7) Wu, F.; Zhao, C.; Chen, S.; Lu, Y.; Hou, Y.; Hu, Y.-S.; Maier, J.; Yu, Y. Multi-Electron Reaction Materials for Sodium-Based Batteries. *Mater. Today* **2018**, *21*, 960−973.

(8) Ortiz-Vitoriano, N.; Drewett, N. E.; Gonzalo, E.; Rojo, T. High Performance Manganese-Based Layered Oxide Cathodes: Overcoming the Challenges of Sodium Ion Batteries. *Energy Environ. Sci.* **2017**, *1*, 151−174.

(9) Eum, D.; Kim, B.; Song, J.-H.; Park, H.; Jang, H.-Y.; Kim, S. J.; Cho, S.-P.; Lee, M. H.; Heo, J. H.; Park, J.; Ko, Y.; Park, S.-K.; Kim, J.; Oh, K.; Kim, D.-H.; Kang, S. J.; Kang, K. Coupling Structural Evolution and Oxygen-Redox Electrochemistry in Layered Transition Metal Oxides. *Nat. Mater.* **2022**, *21*, 664−672.

(10) Wang, Q.-C.; Meng, J.-K.; Yue, X.-Y.; Qiu, Q.-Q.; Song, Y.; Wu, X.-J.; Fu, Z.-W.; Xia, Y.-Y.; Shadike, Z.; Wu, J.; Yang, X.-Q.; Zhou, Y.-N. Tuning P2-Structured Cathode Material by Na-Site Mg Substitution for Na-Ion Batteries. *J. Am. Chem. Soc.* **2019**, *141*, 840−848.

(11) Maitra, U.; House, R. A.; Somerville, J. W.; Tapia-Ruiz, N.; Lozano, J. G.; Guerrini, N.; Hao, R.; Luo, K.; Jin, L.; Pérez-Osorio, M. A.; Massel, F.; Pickup, D. M.; Ramos, S.; Lu, X.; McNally, D. E.; Chadwick, A. V.; Giustino, F.; Schmitt, T.; Duda, L. C.; Roberts, M. R.; Bruce, P. G. Oxygen Redox Chemistry without Excess Alkali-Metal Ions in Na$_{2/3}$[Mg$_{0.28}$Mn$_{0.72}$]O$_2$. *Nat. Chem.* **2018**, *10*, 288−295.

(12) Zhang, K.; Kim, D.; Hu, Z.; Park, M.; Noh, G.; Yang, Y.; Zhang, J.; Lau, V. W.; Chou, S.-L.; Cho, M.; Choi, S.-Y.; Kang, Y.-M. Manganese Based Layered Oxides with Modulated Electronic and Thermodynamic Properties for Sodium Ion Batteries. *Nat. Commun.* **2019**, *10*, 5203.

(13) Shen, Q.; Liu, Y.; Zhao, X.; Jin, J.; Song, X.; Wang, Y.; Qu, X.; Jiao, L. Unexpectedly High Cycling Stability Induced by a High Charge Cut-Off Voltage of Layered Sodium Oxide Cathodes. *Adv. Energy Mater.* **2023**, *13*, No. 2203216.

(14) Ren, H.; Li, Y.; Ni, Q.; Bai, Y.; Zhao, H.; Wu, C. Unraveling Anionic Redox for Sodium Layered Oxide Cathodes: Breakthroughs and Perspectives. *Adv. Mater.* **2022**, *34*, No. 2106171.

(15) Zhang, X.; Qiao, Y.; Guo, S.; Jiang, K.; Xu, S.; Xu, H.; Wang, P.; He, P.; Zhou, H. Manganese-Based Na-Rich Materials Boost Anionic Redox in High-Performance Layered Cathodes for Sodium-Ion Batteries. *Adv. Mater.* **2019**, *31*, No. 1807770.

(16) Kong, W.; Yang, W.; Ning, D.; Li, Q.; Zheng, L.; Yang, J.; Sun, K.; Chen, D.; Liu, X. Tuning Anionic/Cationic Redox Chemistry in a P2-Type Na$_{0.67}$Mn$_{0.5}$Fe$_{0.5}$O$_2$ Cathode Material via a Synergic Strategy. *Sci. China Mater.* **2020**, *63*, 1703−1718.

(17) Sathiya, M.; Rousse, G.; Ramesha, K.; Laisa, C. P.; Vezin, H.; Sougrati, M. T.; Doublet, M.-L.; Foix, D.; Gonbeau, D.; Walker, W.; Prakash, A. S.; Ben Hassine, M.; Dupont, L.; Tarascon, J.-M. Reversible Anionic Redox Chemistry in High-Capacity Layered-Oxide Electrodes. *Nat. Mater.* **2013**, *12*, 827−835.

(18) Saubanère, M.; McCalla, E.; Tarascon, J.-M.; Doublet, M.-L. The Intriguing Question of Anionic Redox in High-Energy Density Cathodes for Li-Ion Batteries. *Energy Environ. Sci.* **2016**, *9*, 984−991.

(19) Xie, Y.; Saubanère, M.; Doublet, M.-L. Requirements for Reversible Extra-Capacity in Li-Rich Layered Oxides for Li-Ion Batteries. *Energy Environ. Sci.* **2017**, *10*, 266−274.

(20) Ben Yahia, M.; Vergnet, J.; Saubanère, M.; Doublet, M.-L. Unified Picture of Anionic Redox in Li/Na-Ion Batteries. *Nat. Mater.* **2019**, *18*, 496−502.

(21) Zhao, C.; Li, C.; Liu, H.; Qiu, Q.; Geng, F.; Shen, M.; Tong, W.; Li, J.; Hu, B. Coexistence of $(O_2)^{n-}$ and Trapped Molecular O_2 as the Oxidized Species in P2-Type Sodium 3d Layered Oxide and Stable Interface Enabled by Highly Fluorinated Electrolyte. *J. Am. Chem. Soc.* **2021**, *143*, 18652−18664.

(22) Yang, L.; Li, X.; Liu, J.; Xiong, S.; Ma, X.; Liu, P.; Bai, J.; Xu, W.; Tang, Y.; Hu, Y.-Y.; Liu, M.; Chen, H. Lithium-Doping Stabilized High-Performance P2-$Na_{0.66}Li_{0.18}Fe_{0.12}Mn_{0.7}O_2$ Cathode for Sodium Ion Batteries. *J. Am. Chem. Soc.* **2019**, *141*, 6680−6689.

(23) Xu, J.; Lee, D. H.; Clément, R. J.; Yu, X.; Leskes, M.; Pell, A. J.; Pintacuda, G.; Yang, X.-Q.; Grey, C. P.; Meng, Y. S. Identifying the Critical Role of Li Substitution in P2-$Na_x[Li_yNi_zMn_{1−y−z}]O_2$ ($0 < x, y, z < 1$) Intercalation Cathode Materials for High-Energy Na-Ion Batteries. *Chem. Mater.* **2014**, *26*, 1260−1269.

(24) Zheng, W.; Liu, Q.; Wang, Z.; Wu, Z.; Gu, S.; Cao, L.; Zhang, K.; Fransaer, J.; Lu, Z. Oxygen Redox Activity with Small Voltage Hysteresis in $Na_{0.67}Cu_{0.28}Mn_{0.72}O_2$ for Sodium-Ion Batteries. *Energy Storage Mater.* **2020**, *28*, 300−306.

(25) Wang, P.-F.; Xiao, Y.; Piao, N.; Wang, Q.-C.; Ji, X.; Jin, T.; Guo, Y.-J.; Liu, S.; Deng, T.; Cui, C.; Chen, L.; Guo, Y.-G.; Yang, X.-Q.; Wang, C. Both Cationic and Anionic Redox Chemistry in a P2-Type Sodium Layered Oxide. *Nano Energy* **2020**, *69*, No. 104474.

(26) Wang, Y.; Zhao, X.; Jin, J.; Shen, Q.; Zhang, N.; Qu, X.; Liu, Y.; Jiao, L. Low-Cost Layered Oxide Cathode Involving Cationic and Anionic Redox with a Complete Solid-Solution Sodium-Storage Behavior. *Energy Storage Mater.* **2022**, *47*, 44−50.

(27) Bai, X.; Sathiya, M.; Mendoza-Sánchez, B.; Iadecola, A.; Vergnet, J.; Dedryvère, R.; Saubanère, M.; Abakumov, A. M.; Rozier, P.; Tarascon, J.-M. Anionic Redox Activity in a Newly Zn-Doped Sodium Layered Oxide P2-$Na_{2/3}Mn_{1−y}Zn_yO_2$ ($0 < y < 0.23$). *Adv. Energy Mater.* **2018**, *8*, No. 1802379.

(28) Zheng, W.; Liang, G.; Zhang, S.; Davey, K.; Guo, Z. Understanding Voltage Hysteresis and Decay During Anionic Redox Reaction in Layered Transition Metal Oxide Cathodes: A Critical Review. *Nano Res.* **2023**, *16*, 3766−3780.

(29) Ding, F.; Wang, H.; Zhang, Q.; Zheng, L.; Guo, H.; Yu, P.; Zhang, N.; Guo, Q.; Xie, F.; Dang, R.; Rong, X.; Lu, Y.; Xiao, R.; Chen, L.; Hu, Y.-S. Tailoring Electronic Structure to Achieve Maximum Utilization of Transition Metal Redox for High-Entropy Na Layered Oxide Cathodes. *J. Am. Chem. Soc.* **2023**, *145*, 13592−13602.

(30) Xu, S.; Wu, J.; Hu, E.; Li, Q.; Zhang, J.; Wang, Y.; Stavitski, E.; Jiang, L.; Rong, X.; Yu, X.; Yang, W.; Yang, X.-Q.; Chen, L.; Hu, Y.-S. Suppressing the Voltage Decay of Low-Cost P2-Type Iron-Based Cathode Materials for Sodium-Ion Batteries. *J. Mater. Chem. A* **2018**, *6*, 20795−20803.

(31) Shen, Q.; Zhao, X.; Liu, Y.; Li, Y.; Zhang, J.; Zhang, N.; Yang, C.; Chen, J. Dual-Strategy of Cation-Doping and Nanoengineering Enables Fast and Stable Sodium-Ion Storage in a Novel Fe/Mn-Based Layered Oxide Cathode. *Adv. Sci.* **2020**, *7*, No. 2002199.

(32) Xiao, Y.; Zhu, Y.-F.; Yao, H.-R.; Wang, P.-F.; Zhang, X.-D.; Li, H.; Yang, X.; Gu, L.; Li, Y.-C.; Wang, T.; Yin, Y.-X.; Guo, X.-D.; Zhong, B.-H.; Guo, Y.-G. A Stable Layered Oxide Cathode Material for High-Performance Sodium-Ion Battery. *Adv. Energy Mater.* **2019**, *9*, No. 1803978.

(33) Li, Y.; Yang, Z.; Xu, S.; Mu, L.; Gu, L.; Hu, Y.-S.; Li, H.; Chen, L. Air-Stable Copper-Based P2-$Na_{7/9}Cu_{2/9}Fe_{1/9}Mn_{2/3}O_2$ as a New Positive Electrode Material for Sodium-Ion Batteries. *Adv. Sci.* **2015**, *2*, No. 1500031.

(34) Cheng, C.; Chen, C.; Chu, S.; Hu, H.; Yan, T.; Xia, X.; Feng, X.; Guo, J.; Sun, D.; Wu, J.; Guo, S.; Zhang, L. Enhancing the Reversibility of Lattice Oxygen Redox Through Modulated Transition Metal-Oxygen Covalency for Layered Battery Electrodes. *Adv. Mater.* **2022**, *34*, No. 2201152.

(35) Zheng, L.; Li, J.; Obrovac, M. N. Crystal Structures and Electrochemical Performance of Air-Stable $Na_{2/3}Ni_{1/3−x}Cu_xMn_{2/3}O_2$ in Sodium Cells. *Chem. Mater.* **2017**, *29*, 1623−1631.

(36) Peng, B.; Chen, Y.; Wang, F.; Sun, Z.; Zhao, L.; Zhang, X.; Wang, W.; Zhang, G. Unusual Site-Selective Doping in Layered Cathode Strengthens Electrostatic Cohesion of Alkali-Metal Layer for Practicable Sodium-Ion Full Cell. *Adv. Mater.* **2022**, *34*, No. 2103210.

(37) Kim, E. J.; Ma, L. A.; Duda, L. C.; Pickup, D. M.; Chadwick, A. V.; Younesi, R.; Irvine, J. T. S.; Armstrong, A. R. Oxygen Redox Activity Through a Reductive Coupling Mechanism in the P3-Type Nickel-Doped Sodium Manganese Oxide. *ACS Appl. Energy Mater.* **2020**, *3*, 184−191.

(38) Cheng, C.; Ding, M.; Yan, T.; Jiang, J.; Mao, J.; Feng, X.; Chan, T.; Li, N.; Zhang, L. Anionic Redox Activities Boosted by Aluminum Doping in Layered Sodium-Ion Battery Electrode. *Small Methods* **2022**, *6*, No. 2101524.

(39) Li, X.-L.; Wang, T.; Yuan, Y.; Yue, X.-Y.; Wang, Q.-C.; Wang, J.-Y.; Zhong, J.; Lin, R.-Q.; Yao, Y.; Wu, X.-J.; Yu, X.-Q.; Fu, Z.-W.; Xia, Y.-Y.; Yang, X.-Q.; Liu, T.; Amine, K.; Shadike, Z.; Zhou, Y.-N.; Lu, J. Whole-Voltage-Range Oxygen Redox in P2-Layered Cathode Materials for Sodium-Ion Batteries. *Adv. Mater.* **2021**, *33*, No. 2008194.

(40) Jin, T.; Wang, P.-F.; Wang, Q.-C.; Zhu, K.; Deng, T.; Zhang, J.; Zhang, W.; Yang, X.-Q.; Jiao, L.; Wang, C. Realizing Complete Solid-Solution Reaction in High Sodium Content P2-Type Cathode for High-Performance Sodium-Ion Batteries. *Angew. Chem., Int. Ed.* **2020**, *59*, 14511−14516.

(41) Wu, Z.; Ni, Y.; Tan, S.; Hu, E.; He, L.; Liu, J.; Hou, M.; Jiao, P.; Zhang, L.; Cheng, F.; Chen, J. Realizing High Capacity and Zero Strain in Layered Oxide Cathodes via Lithium Dual-Site Substitution for Sodium-Ion Batteries. *J. Am. Chem. Soc.* **2023**, *145*, 9596−9606.

(42) Liu, X.; Zuo, W.; Zheng, B.; Xiang, Y.; Zhou, K.; Xiao, Z.; Shan, P.; Shi, J.; Li, Q.; Zhong, G.; Fu, R.; Yang, Y. P2-$Na_{0.67}Al_xMn_{1−x}O_2$: Cost-Effective, Stable and High-Rate Sodium Electrodes by Suppressing Phase Transitions and Enhancing Sodium Cation Mobility. *Angew. Chem., Int. Ed.* **2019**, *58*, 18086−18095.

(43) Wang, C.; Liu, L.; Zhao, S.; Liu, Y.; Yang, Y.; Yu, H.; Lee, S.; Lee, G.-H.; Kang, Y.-M.; Liu, R.; Li, F.; Chen, J. Tuning Local Chemistry of P2 Layered-Oxide Cathode for High Energy and Long Cycles of Sodium-Ion Battery. *Nat. Commun.* **2021**, *12*, 2256.

(44) Voronina, N.; Yu, J. H.; Kim, H. J.; Yaqoob, N.; Guillon, O.; Kim, H.; Jung, M.-G.; Jung, H.-G.; Yazawa, K.; Yashiro; Kaghazchi, P.; Myung, S.-T. Engineering Transition Metal Layers for Long Lasting Anionic Redox in Layered Sodium Manganese Oxide. *Adv. Funct. Mater.* **2023**, *33*, No. 2210423.

(45) Kubota, K.; Asari, T.; Komaba, S. Impact of Ti and Zn Dual-Substitution in P2 Type $Na_{2/3}Ni_{1/3}Mn_{2/3}O_2$ on Ni-Mn and Na-Vacancy Ordering and Electrochemical Properties. *Adv. Mater.* **2023**, *35*, No. 2300714.

(46) Xiao, Z.; Zuo, W.; Liu, X.; Xie, J.; He, H.; Xiang, Y.; Liu, H.; Yang, Y. Insights of the Electrochemical Reversibility of P2-Type Sodium Manganese Oxide Cathodes via Modulation of Transition Metal Vacancies. *ACS Appl. Mater. Interfaces* **2021**, *13*, 38305−38314.

(47) Strauss, F.; Rousse, G.; Alves Dalla Corte, D.; Ben Hassine, M.; Saubanère, M.; Tang, M.; Vezin, H.; Courty, M.; Dominko, R.; Tarascon, J.-M. Electrochemical Activity and High Ionic Conductivity of Lithium Copper Pyroborate $Li_6CuB_4O_{10}$. *Phys. Chem. Chem. Phys.* **2016**, *18*, 14960−14969.

(48) Maurelli, S.; Ruszak, M.; Witkowski, S.; Pietrzyk, P.; Chiesa, M.; Sojka, Z. Spectroscopic CW-EPR and HYSCORE Investigations of Cu^{2+} and $O^{2−}$ Species in Copper Doped Nanoporous Calcium Aluminate ($12CaO·7Al_2O_3$). *Phys. Chem. Chem. Phys.* **2010**, *12*, 10933−10941.

(49) Ji, H.; Ji, W.; Xue, H.; Chen, G.; Qi, R.; Huang, Z.; Fang, H.; Chu, M.; Liu, L.; Ma, Z.; Xu, S.; Zhai, J.; Zeng, W.; Schulz, C.; Wong, D.; Chen, H.; Xu, J.; Yin, W.; Pan, F.; Xiao, Y. Synergistic Activation of Anionic Redox via Co-substitution to Construct High-Capacity Layered Oxide Cathode Materials for Sodium-Ion Batteries. *Sci. Bull.* **2023**, *68*, 65−76.

(50) Li, Z.; Kong, W.; Yu, Y.; Zhang, J.; Wong, D.; Xu, Z.; Chen, Z.; Schulz, C.; Bartkowiak, M.; Liu, X. Tuning Bulk O_2 and Nonbonding Oxygen State for Reversible Anionic Redox Chemistry in P2-Layered Cathodes. *Angew. Chem., Int. Ed.* **2022**, *61*, No. e202115552.

(51) Zou, P.; Yao, L.; Wang, C.; Lee, S. J.; Li, T.; Xin, H. L. Regulating Cation Interactions for Zero-Strain and High-Voltage P2-type $Na_{2/3}Li_{1/6}Co_{1/6}Mn_{2/3}O_2$ Layered Oxide Cathodes of Sodium-Ion Batteries. *Angew. Chem., Int. Ed.* **2023**, *62*, No. e202304628.

(52) Abate, I.; Kim, S. Y.; Pemmaraju, C. D.; Toney, M. F.; Yang, W.; Devereaux, T. P.; Chueh, W. C.; Nazar, L. F. The Role of Metal Substitution in Tuning Anion Redox in Sodium Metal Layered Oxides Revealed by X-Ray Spectroscopy and Theory. *Angew. Chem., Int. Ed.* **2021**, *60*, 10880−10887.

(53) Li, B.; Sougrati, M. T.; Rousse, G.; Morozov, A. V.; Dedryvère, R.; Iadecola, A.; Senyshyn, A.; Zhang, L.; Abakumov, A. M.; Doublet, M.-L.; Tarascon, J.-M. Correlating Ligand-to-Metal Charge Transfer with Voltage Hysteresis in a Li-Rich Rock-Salt Compound Exhibiting Anionic Redox. *Nat. Chem.* **2021**, *13*, 1070−1080.

(54) Huang, J.; Ouyang, B.; Zhang, Y.; Liang, Y.; Kwon, D.-K.; Cai, Z.; Lun, Z.; Zeng, G.; Balasubramanian, M.; Ceder, G. Inhibiting Collective Cation Migration in Li-Rich Cathode Materials as a Strategy to Mitigate Voltage Hysteresis. *Nat. Mater.* **2023**, *22*, 353−361.

(55) Singh, G.; López Del Amo, J. M.; Galceran, M.; Pérez-Villar, S.; Rojo, T. Structural Evolution During Sodium Deintercalation/ Intercalation in $Na_{2/3}[Fe_{1/2}Mn_{1/2}]O_2$. *J. Mater. Chem. A* **2015**, *3*, 6954−6961.

(56) Cao, X.; Li, H.; Qiao, Y.; He, P.; Qian, Y.; Yue, X.; Jia, M.; Cabana, J.; Zhou, H. Reversible Anionic Redox Chemistry in Layered $Li_{4/7}[\square_{1/7}Mn_{6/7}]O_2$ Enabled by Stable Li-O-Vacancy Configuration. *Joule* **2022**, *6*, 1290−1303.

(57) Pei, Y.; Chen, Q.; Ha, Y.; Su, D.; Zhou, H.; Li, S.; Yao, Z.; Ma, L.; Sanders, K. J.; Sheng, C.; Gillian, R. G.; Gu, L.; Yu, A.; Yang, W.; Chen, Z. Fluorinated Rocksalt Cathode with Ultra-High Active Li Content for Lithium-ion Batteries. *Angew. Chem., Int. Ed.* **2022**, *61*, No. e202212471.

(58) Gao, X.; Liu, H.; Chen, H.; Mei, Y.; Wang, B.; Fang, L.; Chen, M.; Chen, J.; Gao, J.; Ni, L.; Yang, L.; Tian, Y.; Deng, W.; Momen, R.; Wei, W.; Chen, L.; Zou, G.; Hou, H.; Kang, Y.-M.; Ji, X. Cationic-Potential Tuned Biphasic Layered Cathodes for Stable Desodiation/ Sodiation. *Sci. Bull.* **2022**, *67*, 1589−1602.

(59) Deng, J.; Luo, W.-B.; Lu, X.; Yao, Q.; Wang, Z.; Liu, H.-K.; Zhou, H.; Dou, S.-X. High Energy Density Sodium-Ion Battery with Industrially Feasible and Air-Stable O3-Type Layered Oxide Cathode. *Adv. Energy Mater.* **2018**, *8*, No. 1701610.

(60) Wang, H.; Pan, Z.; Zhang, H.; Dong, C.; Ding, Y.; Cao, Y.; Chen, Z. A Green and Scalable Synthesis of $Na_3Fe_2(PO_4)$ P_2O_7/rGO Cathode for High-Rate and Long-Life Sodium-Ion Batteries. *Small Methods* **2021**, *5*, No. 2100372.